Oceanic Anoxic Event 3 coincided with peak Caribbean Large Igneous Province volcanism at 88 Ma

Goran Andjić[1]*, Peter O. Baumgartner[1], Claudia Baumgartner-Mora[1], Alexey Ulianov[1], Brahimsamba Bomou[1], László Kocsis[2], Francesco Miniati[3], Marco Chiari[3]

[1]*Institute of Earth Sciences, University of Lausanne, Géopolis, 1015 Lausanne, Switzerland*
[2]*Institute of Earth Surface Dynamics, University of Lausanne, Géopolis, 1015 Lausanne, Switzerland*
[3]*Institute of Geosciences and Earth Resources (IGG), National Research Council of Italy (CNR), Via G. La Pira, 4, 50121 Firenze, Italy*

**Corresponding author: goran.andjic@unil.ch*

Highlights

- Black shales from the Loma Chumico Formation date to 88–87 Ma.
- Black shale deposition matches the onset of OAE3 and peak volcanism of the CLIP.
- Mercury spikes from Holes 700B and U1513A, calibrated with carbon isotope data, suggest LIP volcanism shortly before and during OAE3.
- Combined stratigraphic, geochronological, and geochemical data suggest a causal link between CLIP magmatism and OAE3.

Abstract

The high-volume, short-lived magma flux associated with the eruption of oceanic large igneous provinces (LIPs) is believed to have triggered Cretaceous Oceanic Anoxic Events, most notably OAE1 (~120–100 Ma) and OAE2 (~94 Ma). In contrast, OAE3 (~88–84 Ma) is considered to have occurred independently of LIP volcanism. Here we present a record of OAE3-related black shale deposition in Costa Rica that is coeval with the peak phase of the Caribbean LIP. Radiolarian biostratigraphy and zircon U-Pb geochronology from the Loma Chumico Formation indicate that black shale formation in the Costa Rican forearc was synchronous with the onset of OAE3 at around 88 Ma. Recently revised $^{40}Ar/^{39}Ar$ ages of LIPs show that the Caribbean LIP is the best candidate to hypothesize a causal link between OAE3 and a major magmatic event. Peak volcanism of the Caribbean LIP between 88 and 86 Ma occurred at the same time as global carbon cycle perturbations in marine and terrestrial settings, as well as oceanic anoxia. New mercury records, calibrated with carbon isotopes and used as a proxy for LIP volcanism, from ODP Hole 700B and IODP Hole U1513A suggest that the Caribbean LIP not only coincided with OAE3 but may have actually triggered it. Overall, these new and existing data suggest a significant role of the Caribbean LIP in driving environmental and climatic perturbations during the Coniacian–Santonian.

1. Introduction

Oceanic Anoxic Events (OAEs) represent major disruptions in Earth's climate and carbon cycle, typically marked by widespread oceanic anoxia and deposition of organic-rich black shales (Leckie et

al., 2002). These events were primarily triggered by rapid global warming caused by large releases of CO_2 from volcanic sources, most likely large igneous provinces (LIPs; e.g., Kuroda et al., 2007; Barclay et al., 2010). LIP-induced warming accelerated the hydrological cycle, increased continental weathering, intensified wind-driven upwelling, and boosted nutrient runoff into oceans, leading to enhanced biological productivity and organic matter deposition (Jenkyns, 2010). Disturbances in the carbon cycle were recorded through carbon isotopes ($\delta^{13}C$), while geochemical proxies of volcanism–such as osmium isotopes and mercury (Hg) abundances–may be used to infer links between LIP eruptions and global environmental changes (Turgeon and Creaser, 2008; Percival et al., 2024).

Considered as the last OAE in Earth's history, OAE3 was a relatively low-amplitude perturbation of the global carbon cycle that occurred during the Coniacian–Santonian (~89.8–83.6 Ma; Jenkyns, 1980; Wagreich, 2009). Modest positive $\delta^{13}C$ excursions (≤~1‰) associated with OAE3 have been documented globally, from low to high latitudes, in both marine and terrestrial records (Wagreich, 2012; Richey et al., 2023). OAE3 was typically expressed as organic-rich black shales in many near-continental and epicontinental seas (Fig. 1) and resulted in regional anoxia and extinction of benthic foraminifera (Mansour and Wagreich, 2022). Unlike earlier Cretaceous OAEs, OAE3 is not thought to have been triggered by any of the LIPs active during the Coniacian–Santonian, mainly because: (i) the OAE3 is not confined to a single, well-defined black shale interval, but rather consists of distinct subevents (e.g., Wagreich, 2009); and (ii) no significant LIP activity is thought to have occurred during that time (e.g., Kerr, 2014). Instead, black shale deposition has been interpreted as largely driven by regional paleogeographic conditions, which modulated the accumulation and preservation of organic matter during OAE3 (Mansour and Wagreich, 2022).

Until recently, the eruptions of the Caribbean Large Igneous Province (CLIP) were regarded as one of the principal causes of the Cenomanian–Turonian Boundary Event or OAE2 (e.g. Scaife et al., 2017; Percival et al., 2024), because the CLIP was considered the largest single expression of magmatism on Earth at that time (Snow et al., 2005; Coffin et al., 2006). As discussed in this paper, the main CLIP activity (~94–63 Ma; Loewen et al., 2013) may have been actually too young to have significantly contributed to the climate change of the OAE2 (~94 Ma), as already noted by Kasbohm et al. (2021). Radiolarian biostratigraphic work (e.g., Baumgartner et al., 2008) has repeatedly documented Coniacian–Santonian radiolarian assemblages from radiolarites interbedded between lava flows of the CLIP in the Nicoya Complex (northeast Nicoya Peninsula, Costa Rica). In the Nicoya Complex, alternations of green radiolarian cherts and black shales overlain by CLIP basalts dated as 92–83 Ma, document OAE3 anoxia in a Paleo-Pacific oceanic environment (Baumgartner et al., 2024). Radiolarites in stratigraphic contact with CLIP basalts of the Azuero Plateau (Panama) yielded similar Coniacian–Santonian assemblages (Kolarsky et al., 1995). Possible OAE3 sediments, studied for their source rock potential (Carvajal-Arenas et al., 2020) were found at DSDP Sites 146, 151, and 153, located on Beata Ridge and in the eastern Caribbean basin (Fig. 1), where layers rich in radiolarians and organic matter associated with basalt flows of the CLIP roof were recovered. These basalts have yielded $^{40}Ar/^{39}Ar$ ages of 92.1 ± 4.7 and 90.6 ± 3.2 Ma, which coincide with those obtained between 92.4 and 76.9 Ma for igneous rocks dredged from the Beata Ridge (Dürkefälden et al., 2019). Planktonic foraminifera present in sandstones overlying CLIP basalts in site 153 define the *Marginotruncana schneegansi* zone of upper Turonian age (Edgar et al., 1973).

Recent advances in the statistical treatment of $^{40}Ar/^{39}Ar$ age data of LIPs (Jiang et al., 2023), along with the documentation of elevated Hg abundances in organic-rich rocks from OAE3 (Grasby et al., 2025),

make it timely to reevaluate whether OAE3 was a "LIP-less" event. In this paper, we combine radiolarian biostratigraphy and zircon U-Pb geochronology to refine the age of Costa Rican black shales that overlie accreted remnants of the CLIP and were previously attributed to OAE3 (Andjić et al., 2019; Fig. 1). We then use these new time constraints to assess whether the OAE3 black shales coincide with the revised ages of the CLIP and other LIPs. Moreover, we assess whether LIP activity was synchronous with OAE3 through Hg analyses from ODP Hole 700B and IODP Hole U1513A, as Hg enrichments would be expected globally in marine sediments if a major LIP eruption occurred at that time. Overall, clarifying this relationship is important for evaluating whether LIP activity played a more significant role in triggering the OAE3 than previously recognized, and more broadly, for understanding the drivers of Late Cretaceous global carbon cycle perturbations and oceanic anoxia.

2. Geological setting

2.1. Loma Chumico Fm. (Costa Rica)

The Loma Chumico Formation (Fm.) is a deep-water, volcaniclastic-dominated formation deposited in the Tempisque forearc basin (Andjić et al., 2019), reflecting the activity of an intraoceanic arc in northern Costa Rica during the Coniacian–Campanian (~89–75 Ma; Bandini et al., 2008; Andjić et al., 2018; Fig. 2). The Loma Chumico Fm. is divided into two parts: a lower, silica- and organic-rich part (Coniacian–Santonian) and an upper, carbonate-rich part (Campanian; Andjić et al., 2019). This change in facies is interpreted as a response to a global reorganization of deep-water circulation, which shifted towards more oligotrophic conditions during the Campanian (Erlich et al., 1996; Andjić et al. 2019). The black shales of the Loma Chumico Fm., which contain an average total organic carbon of ~16 wt.% (Erlich et al., 1996), have been dated to the Coniacian–Santonian using interbedded radiolarian-rich volcaniclastic rocks (Andjić et al., 2018, 2019). The Loma Chumico Fm. overlies a mafic basement primarily composed of basalts, which are intruded by dolerites and gabbros. With formation ages between 94 and 89 Ma, and geochemical signatures consistent with plume-derived magmatism, these mafic rocks are considered typical of the CLIP (e.g., Hauff et al., 2000). They were likely accreted to the margin of what is now Costa Rica as a result of the collision between the northern edge of the CLIP and the North American plate during the early Coniacian (Manzanillo Terrane in Andjić et al., 2019; Fig. 1).

2.2. ODP Hole 700B and IODP Holes U1513

Hole 700B was drilled on the northeastern slope of the Northeast Georgia Rise in the South Atlantic (Fig. 1; Ciesielski and Kristoffersen, 1988). The studied interval, extending from 450 to 483 m below seafloor (mbsf), was sampled between cores 51R and 54R and spans an age range from the earliest Santonian to the Coniacian (Petrizzo et al., 2020). Only core 51R shows no recovery gaps among the drilled cores. The drilled lithology consists of micritic limestone alternating with clay-bearing to clayey micritic limestone. Dispersed, discrete ash-rich layers are present within the sampled interval, generally measuring 1–3 cm in thickness.

Holes U1513A, U1513B, and U1513D were drilled on the eastern slope of the Naturaliste Plateau off the southwestern margin of Australia (southeast Indian Ocean; Huber et al., 2019; Fig. 1). Data from Holes U1513 are plotted on the CCSF depth scale (core composite depth below sea floor). The studied interval, extending from 97.35 to 186.44 m CCSF spans an age range from the earliest Santonian to the

latest Turonian (Huber et al., 2019: Petrizzo et al., 2022); it was sampled between cores 17X and 32X in Hole U1513A, in core 14F in Hole U1513B, and between cores 6R and 11R in Hole U1513D. The recovery of cores is generally low. The drilled lithology consists of calcareous and nannofossil oozes gradually transitioning into nannofossil chalk between 130 and 170 m CCSF. Irregular nodules of white to grey silicified limestone are common throughout the studied cores.

3. Materials and methods

To test the temporal correlation between the studied organic-rich intervals, OAE3, and CLIP volcanism, we applied a field-based geochronological and biostratigraphic approach, building on the regional stratigraphic work of Andjić et al. (2018, 2019). We studied a composite section of the lower Loma Chumico Formation in three localities of the southeastern Nicoya Peninsula (Fig. 2A): Loma Chumico (N 10°03'44.5''/W 85°15'52.4''), Punta Pochote (N 09°44'44.9''/W 84°59'30.6''), and Bahia Murciélago (N 09°44'46.9''/W 84°57'19.3''). Zircon U-Pb geochronology and radiolarian biostratigraphy were used to date tuffs and volcaniclastic rocks interbedded with black shales of the Loma Chumico Fm. In addition, Hg abundances of carbonates from Hole 700B (S 51°31'58.6''/W 30°16'41.3'') and Hole U1513A (S 33°47'36.5''/E 112°29'8.1'') were obtained in combination with carbon stable isotopes and total organic carbon contents to further evaluate the coincidence between OAE3 and CLIP volcanism.

3.1.U-Pb dating of zircon by LA-ICP-MS

Three tuffs and three volcaniclastic rocks (each <1 kg) were crushed using a hydraulic press, then milled in a tungsten shatterbox and sieved to a grain size of <250 µm. The sieved material was panned to remove the lightest fraction, then dried in an oven at 70°C for 24 hours. Heavy minerals were separated with a Frantz magnetic separator, and gravimetric separation was carried out using methylene iodide. Between six and thirty-nine zircon crystals per sample were selected using a binocular microscope. Grains of similar size were handpicked and mounted on 25 mm epoxy pucks, and manually polished to expose grain centers. The internal structure of the zircons was investigated by cathodoluminescence (CL) imaging, using a CamScan MV2300 scanning electron microscope at the Institute of Earth Sciences, University of Lausanne.

U–Pb ages of zircon grains were obtained by laser ablation inductively coupled plasma mass spectrometry (LA-ICP-MS). Measurements were carried out using an Element XR sector-field single collector ICP-MS (Thermo Scientific) interfaced to a RESOlution-SE excimer 193 nm ablation system equipped with a S155 two-volume ablation cell (Australian Scientific Instruments/Applied Spectra) at the Institute of Earth Sciences, University of Lausanne. The laser spot diameter was set at 20 µm. A low on-sample energy density of 2.3 J/cm^2, a slow repetition rate of 5 Hz, and a short ablation time (12 s signal duration) were used to minimize isotopic fractionation (Ulianov et al., 2012). The GJ-1 reference zircon (600.36 Ma; Boekhout et al., 2012; Ulianov et al., 2012) was used as a primary standard for the calibration of the relative sensitivities. The Plešovice reference zircon (337.13 ± 0.37 Ma; Sláma et al., 2008) was used as a secondary standard. Data reduction was done in LAMTRACE. Normal concordia and weighted mean age diagrams were calculated using IsoplotR (Vermeesch, 2018). The weighted mean $^{206}Pb/^{238}U$ age of the Plešovice zircon during the session amounted to 337.80 ± 0.64 Ma (MSWD = 1.1, n = 47). All data are displayed in Table S1; analyses that appear visually discordant in concordia diagrams (Fig. S1) are excluded from interpretations.

In the results section, weighted mean ages are reported in the notation: age ± [X], where [X] represents the internal (analytical) uncertainty derived from data scatter alone, excluding systematic (external) uncertainties. Thus, [X] provides a minimum estimate of the full uncertainty on the mean age. Based on years of analysis using standards and samples with known ID-TIMS ages, the maximum total uncertainty of our LA-ICP-MS laboratory is estimated at 1.6% (2s) of the ID-TIMS ages (Noroña Muñoz et al., 2025). To estimate the maximum full uncertainty of a given sample, the internal and systematic uncertainties can be propagated assuming zero covariance, using the formula: $\sqrt{(a)^2 + (b)^2}$ (a = analytical uncertainty [X], b = 1.6% maximum systematic uncertainty).

3.2. Radiolarian extraction and dating

Radiolarians were previously extracted by Andjić et al. (2018, 2019), who detailed an extraction method involving hydrofluoric and hydrochloric acids. In the present study, radiolarians were picked from existing residues of five samples. By combining new and previously illustrated material with recent advances in radiolarian biostratigraphy (O'Dogherty et al., 2009: Bragina et al., 2021; Baumgartner et al., 2024; Bragina, 2025), we were able to refine the radiolarian age determinations from the earlier studies by Andjić et al. (2018, 2019). The new material was imaged using a Tescan Mira II LMU scanning electron microscope equipped with a secondary electron detector at the Institute of Earth Sciences, University of Lausanne.

3.3. Stable isotope compositions

Oxygen and carbon isotope analyses (112 samples) were conducted in the stable isotope laboratory of the Institute of Earth Surface Dynamics at the University of Lausanne with a Gas-Bench Plus sample introduction system interfaced to a Thermo Fisher Scientific Delta V Plus isotope ratio mass spectrometer following the method described in Spötl and Vennemann (2003). The stable carbon and oxygen isotope ratios are expressed in delta notation as per mil (‰) relative to the Vienna Pee Dee Belemnite (VPDB) international reference standard. Multiple analyses of an in-house standard (Carrara marble, calibrated to international carbonate standards of NBS-18 and NBS-19) were run parallel with the samples to correct raw isotopic values. The analytical precision of the method is better than ±0.1 ‰ (1s) for both C- and O-isotope compositions. The results are presented in Table S2.

3.4. Mercury (Hg) and total organic carbon (TOC)

Hg was quantified using a Zeeman R-915F high-frequency atomic absorption spectrometer (Lumex, St-Petersburg, Russia) at the Institute of Earth Sciences, University of Lausanne. Whole rock powder samples (n = 78) were weighted into a glass measuring boat and then placed into the pyrolizer set at 700°C to evaporate the Hg and determine its concentration in ppb. Measurements were done in duplicates when enough material was available (i.e., Hole U1513A). A certified external standard (BCR-277R, Hg = 128 ppb) was used for calibration purposes. The method detection limit is 0.5–3.0 ppb. TOC contents were measured on 74 samples using a Rock EvalTM 6 at the same institution as above. The instrument was calibrated using the IFP160000 standard with an instrumental precision of <0.1 wt.% for TOC. TOC normalization was applied to Hg values; however, due to very low TOC contents (<0.2 wt%), Hg/TOC values were not used in our interpretations to avoid potential errors

associated with near-detection-limit TOC values (e.g., Grasby et al., 2019). The results are presented in Table S2.

4. Results

4.1. Lithostratigraphy of the lower Loma Chumico Fm.

The studied sections of the lower Loma Chumico Fm. consist predominantly of radiolarian-bearing volcaniclastic beds. In Punta Pochote and Bahia Murciélago, the Loma Chumico Fm. overlies a basaltic basement composed of hyaloclastites and pillow basalts (Fig. 2). All the sections are dominated by (sandy) tuffaceous siltstones, which are locally interbedded with tuffs (Fig. S2A), sandstones (Fig. S2E), breccias, and conglomerates. Tuffs are composed of vitric ash exhibiting cuspate glass shards in a glassy matrix (Fig. S2B, S2C). Sandstones are made of feldspars, pyroxenes, and Fe-Ti oxides set in a silt-sized tuffaceous matrix. Millimeter- to centimeter-sized rip-up clasts of tuffaceous siltstone are common in the sandstones, suggesting transport of volcaniclastic material on the seafloor. A several-meter-thick interval of black shales (Fig. S2D) is present in the Loma Chumico and Punta Pochote sections (Fig. 2C). In the latter section, black shale-tuffaceous siltstone alternations also occur as meter-scale rip-up clasts within basaltic debris flows. Outcrops in Punta Pochote and Bahía Murciélago indicate that black shales do not overlie the basaltic basement in the southernmost Nicoya Peninsula, unlike in the central Nicoya Peninsula–where such an overlying relationship is documented in the Río Blanco (~5 km southwest of Loma Chumico; Andjić et al., 2019; Fig. 2B). Based on stratigraphic relationships and age constraints presented below, the deposition of black shales of the Loma Chumico Fm. can be restricted to the middle to late Coniacian.

4.2. Zircon U-Pb ages of tuff and detrital samples (Loma Chumico Fm.)

Zircons were recovered from three centimeter-thick tuff layers (Figs. 2C and S2). Within each sample, zircon crystals appear consistently clear, colorless, and euhedral under transmitted light, suggesting origin from a single volcanic source. Most of the zircon grains are relatively equant and typically <100 μm wide, whereas less common elongate zircons are generally <100 μm long. The weighted means of the analyzed zircons are interpreted below as the depositional ages.

Sample MUC20 from the Bahia Murciélago section yielded 6 concordant analyses with a weighted mean age of 90.0 ± 1.7 Ma (2s, n = 6, MSWD = 1.7; Fig 3). This U-Pb zircon age is, within uncertainty, consistent with the $^{87}Sr/^{86}Sr$ age of 88.4–89.1 Ma (calibrated to the timescale of Ogg et al., 2016 and based on the $^{87}Sr/^{86}Sr$ curve of McArthur and Howarth, 2020), which was obtained by Weber (2013) from an *Inoceramus* shell (sample MUC13, $^{87}Sr/^{86}Sr$ = 0.707349 ± 0.000003) collected 30 m above sample MUC20 (Fig. 2C). Moreover, it is in accordance with the Coniacian age obtained from radiolarian sample MUC12.

Samples LCH15-00 and LCH15-04 from the Loma Chumico section yielded 16 and 35 concordant analyses, respectively. Sample LCH15-00 is interstratified with black shales and has a weighted mean age of 87.08 ± 0.94 Ma (2s, n = 16, MSWD = 1.4). Sample LCH15-04 is located ~ 9 m above the black shales; after removing three zircon analyses due to discordance, the data yields a weighted mean age of

87.38 ± 0.76 Ma (2s, n = 35, MSWD = 0.49). Both U-Pb zircon ages overlap with the middle to late Coniacian age derived from radiolarian samples LCH0 and LCH15-03.

Detrital zircons were separated from three centimeter-sized volcaniclastic rocks collected in the Punta Pochote section (Figs. 2C and S2). Within each sample, the zircon crystals appear consistently clear, colorless, and euhedral under transmitted light. Within each sample, the proportion of equant and elongate zircon grains is relatively similar, with sizes typically <120 μm. The weighted means of the analyzed zircons are interpreted below as the maximum depositional ages, following the YC2σ(3+) method of Dickinson and Gehrels (2009), in which the weighted mean is calculated from the youngest three or more dates that overlap within 2s analytical uncertainty.

Sample CRPC05 was collected from a coarse-grained sandstone located 1.5 m above the basaltic basement and ~60 m below the main black shale interval (Fig. 2C); it yields a weighted mean age of 88.6 ± 0.4 Ma (1s, n = 23, MSWD = 1.2; Fig. 3). Sample 1PCH4 was collected from a meter-scale rip-up clast composed of alternating sandy tuffaceous siltstone and black shale; after removing one analysis due to discordance, the data yield a weighted mean age of 88.0 ± 1.5 Ma (1s, n = 3, MSWD = 2.6). Sample PCH14-02 was collected from a fine-grained sandstone 1 m below the main black shale interval; after removing two analyses due to discordance, the data yield a weighted mean age of 89.2 ± 0.4 Ma (1s, n = 11, MSWD = 1.4). The maximum depositional ages of samples CRPC05, 1PCH4, and PCH14-02 are consistent with the ages of radiolarian samples CRCP03 (middle to late Coniacian) and 1PCH7B (Coniacian). This supports the geological significance of the weighted mean ages derived from detrital zircons, despite the relatively small sample size (n).

4.3. Radiolarian biostratigraphy of the Loma Chumico Fm.

Age-diagnostic radiolarians were extracted from five samples collected in the lower Loma Chumico Fm. (Figs. 1, 2, 4). Here we mention only the species that were key to assign an age to the studied samples; the full assemblages are reported in Fig. 4. For sample CRPC03 (Punta Pochote), which was collected from the stratigraphically lowermost part of the Loma Chumico Fm., a middle to late Coniacian age is deduced from the following co-occurrence: *Annikaella omanensis* (first occurrence in the middle to late Coniacian) associated with *Archaeospongoprunum venadoensis*, *Hemicryptocapsa polyhedra,* and *Pseudoaulophacus putahensis* (last occurrence in Coniacian). For sample 1PCH7B (Punta Pochote), a Coniacian age is deduced from the following co-occurrence: *Alievium gallowayi, Alievium praegallowayi, Dictyoprora salillum, Dictyoprora tina, Dictyoprora urna,* and *Pseudodictyomitra crassa* (first occurrence in Coniacian) associated with *Hemicryptocapsa polyhedra* and *Pseudoaulophacus putahensis* (last occurrence in Coniacian). For sample MUC12 (Bahia Murciélago), a Coniacian age is deduced from the following co-occurrence: *Alievium gallowayi, Dictyoprora ascalia, Dictyoprora salillum, Pseudodictyomitra crassa* and *Pseudodictyomitra tiara* (first occurrence in Coniacian) associated with *Hemicryptocapsa polyhedra* (last occurrence in Coniacian). For sample LCH15-03 (Loma Chumico), a middle to late Coniacian age is deduced from the following co-occurrence: *Annikaella omanensis* (first occurrence in the middle Coniacian) associated with *Hemicryptocapsa polyhedra* (last occurrence in Coniacian). For sample LCH0 (Loma Chumico), a middle to late Coniacian age is deduced from the following co-occurrence: *Annikaella omanensis* (first occurrence in the middle Coniacian) associated with *Hemicryptocapsa polyhedra* and *Pseudoaulophacus putahensis* (last occurrence in Coniacian).

4.4. ODP Hole 700B and IODP Holes U1513: $\delta^{13}C_{carb}$, Hg and TOC

In the studied cored interval of Hole 700B, $\delta^{13}C_{carb}$ values have a range between 2.1 ‰ and 3.1 ‰ (Fig. 5A). Based on two key planktonic foraminifera datums identified by Petrizzo et al. (2020), we correlate the carbon isotope curve of Hole 700B with that of the English Chalk (Jarvis et al., 2006; Miniati et al., 2025; Fig. S4). The lowest occurrence of *Globotruncana linneiana* is used to constrain the position of the Coniacian–Santonian boundary (~86.3 Ma) between 456.41 and 457.91 mbsf, while the lowest occurrence of *Planoheterohelix papula* is used to constrain the position of the early late Coniacian (~87.8 Ma) between 471.11 and 474.12 mbsf (Petrizzo et al., 2020). Therefore, we correlate the positive carbon anomaly at 463.48 mbsf with the Kingsdown event, while the positive carbon anomaly at 475.97 mbsf is correlated with the White Fall event. The negative carbon isotope anomaly at 480.44–481.35 mbsf is correlated with the East Cliff event. Hg abundances range between 0 and 10.6 ppb and do not show any correlation with $CaCO_3$ (~60–82 wt%) and TOC (~0.08–0.38 wt%) contents. The highest Hg value (10.6 ppb) at 483.10 mbsf immediately precedes the East Cliff event. Despite the noise in the curve, we observe an overall decrease in Hg contents through the studied interval towards the Coniacian–Santonian boundary.

In the studied cored interval of Holes U1513A, U1513B, and U1513D, $\delta^{13}C_{carb}$ values have a range between 2.6 ‰ and 3.7 ‰ (Fig. 5B). Based on one key calcareous nannofossil and one key planktonic foraminifera datums (Huber et al., 2019; Petrizzo et al., 2022), we correlate the carbon isotope curve of Holes U1513 with that of the English Chalk (Jarvis et al., 2006; Miniati et al., 2025; Fig. S4). The lowest occurrence of the planktonic foraminifera *Globotruncana linneiana* is used to constrain the position of the Coniacian–Santonian boundary (~86.3 Ma) at 104.45 m CCSF. The Turonian–Coniacian boundary (~89.8 Ma) is placed at 180 m CCSF, based on the lowest occurrence of the calcareous nannofossil *Micula staurophora* at 166.98 m CCSF, as follows. In the recently revised nannofossil scheme for the English Chalk (Miniati et al., 2025), the lowest occurrence of *Micula staurophora* occurs in the lower Coniacian between the East Cliff and the Light Point events. We identify these events at 154.88–157.26 m CCSF and 172.9 m CCSF, respectively, in the new carbon isotope curve of Holes U1513. Therefore, the negative anomaly preceding these positive excursions (180.06–186.44 m CCSF) is interpreted as the Navigation event, marking the latest Turonian. Moreover, we identify the Kingsdown event at 139.31 m CCSF and the White Fall event at 149.63 m CCSF. Hg abundances from Hole U1513A range between 5.5 and 129.3 ppb and do not show any correlation with $CaCO_3$ (~18.6–84.2 wt%). A weak positive correlation exists between Hg and TOC (~0.05–0.24 wt%) values; however, such low TOC values are insufficient to reliably interpret Hg–organic matter associations (e.g., Grasby et al., 2019). The highest Hg values (116.2 and 129.3 ppb) at 158.33–158.77 m CCSF form a distinct peak that immediately precedes the East Cliff event. Additionally, a secondary peak (90 ppb) at 148.37 m CCSF appears immediately after the White Fall event. Although the curve shows some noise, Hg content decreases toward the Coniacian–Santonian boundary.

5. Discussion

5.1. Correlation between Loma Chumico black shales and OAE3

To evaluate the temporal correlation between the Loma Chumico black shales and OAE3, we first examine the timing of the OAE3 subevents. Based on compiled geochemical and isotope proxy data from ~100 sections, Mansour and Wagreich (2022) reported the age ranges of three globally recognized

subevents within the Coniacian–Santonian OAE3: (a) 87.1–86.6 Ma; (b) 85.5–84.7 Ma; (c) 84.0–83.5 Ma. Given that our new data constrain the age of the Loma Chumico black shales to the middle to late Coniacian, we focus here on their correlation with the OAE3a subevent.

We emphasize that the duration and timing of OAE3a, as defined by Mansour and Wagreich (2022), are not widely accepted. (i) A consensus has not been reached on the absolute ages of the Turonian–Coniacian and Coniacian–Santonian boundaries (e.g., Thibault et al., 2016; Mansour and Wagreich, 2022; Bomou et al., 2025; Singer et al., 2025). The timescale used to calibrate the carbon isotope curves in the Turonian–Campanian interval may thus shift the age of the OAE3a up to ~0.4 Ma. (ii) Basin restriction and local environmental factors may have influenced both the recorded duration and facies expression of OAE3a. For example, OAE3a is interpreted to have begun ~0.6 Ma earlier in the Western Interior Seaway (Joo and Sageman, 2014; Grasby et al., 2025; Fig. 6) than in the English Chalk (Mansour and Wagreich, 2022), and was accompanied by black shale deposition only in the former.

Nevertheless, whichever timescale and subevent duration are preferred, the age of the Loma Chumico black shales overlaps with that of the OAE3a. In particular, our most robust detrital zircon age (sample CRPC05), the tuff zircon age from Bahia Murciélago (sample MUC20), the radiolarian sample CRPC03 (Punta Pochote), and the $^{87}Sr/^{86}Sr$ data from Weber (2013)–all from lithologies underlying the black shale interval–indicate that black shale deposition may have started from 88.4–87.8 Ma (Figs. 2 and 6). Combining all our zircon ages from rocks encompassing the organic-rich interval of the Loma Chumico Fm. into a single Kernel Density Estimation (KDE) curve yields a single peak at 87.8 Ma (Fig. 6c). These ages are supported by the middle to late Coniacian radiolarian age (~88.4–86.3 Ma) of tuffaceous siltstones interbedded with black shales in the Loma Chumico section (Figs. 2, 4, 6), which also rules out the Santonian as a possible depositional age. It cannot be confidently determined from our dataset whether the bulk of the Loma Chumico black shales was deposited around 88 Ma (i.e., Western Interior Seaway; Joo and Sageman, 2014) or slightly later, around 87.4 Ma (i.e., Mansour and Wagreich, 2022).

In sections where OAE3a is expressed as black shales, their total thickness commonly ranges between 5 and 20 m (e.g., De Romero et al., 2003; Joo and Sageman, 2014; Prauss, 2015; Tessin et al., 2015). This range aligns well with our field observations of the Loma Chumico black shales, which generally show a total thickness of less than 20 m. However, borehole data from Erlich et al. (1996) provide a more complex picture. The Morote-1 core, drilled a few kilometers east of the Loma Chumico section (Fig. 2A), shows a combined black shale thickness reaching 85 m. Within the Morote-1 well, individual black shales intervals reach thicknesses of up to 14 m, comparable to that observed in the Loma Chumico section. Moreover, the Manzanillo-1 well (Fig. 2A), located on the eastern side of Nicoya Gulf, penetrated three organic-rich intervals, with the lowermost measuring roughly 25 m thick and the others about half that thickness. The simplest explanation to these observations is that the Loma Chumico Fm. may have recorded all three subevents of the OAE3. Although Erlich et al. (1996) did not mention this possibility, the average 70% core recovery from the Manzanillo-1 and Morote-1 wells may have concealed thrusts and faults that could have caused repetitions in the subsurface Loma Chumico Fm. Such tectonic complications were observed by us in the Loma Chumico section and acknowledged by Erlich et al. (1996). Nevertheless, repetitions of the black shale intervals in the Manzanillo-1 well seem unlikely, as the three distinct intervals include one that is roughly twice the thickness of the others. Indeed, the interplay between local and global factors may have contributed to prolonged black shale deposition during and between the subevents of the Coniacian–Santonian OAE3 (Erlich et al., 1996;

Tessin et al., 2015; Andjić et al., 2019). Further geochronological and biostratigraphic work in the Loma Chumico Fm. is needed to test these hypotheses.

5.2. Correlation between OAE3 and CLIP volcanism

A causal relationship between environmental perturbations, black shale deposition, and LIP eruptions has been well established for the Cretaceous OAE1 and OAE2 (e.g., Ernst and Youbi, 2017; Kasbohm et al., 2021). However, a similar connection for OAE3 has remained elusive, largely because it was long assumed that no major intraplate volcanism occurred during the late Coniacian–Santonian interval (88–84 Ma; e.g., Kerr, 2014). The most plausible candidate linking a LIP to OAE3 is the CLIP, whose eruption ages span this time window. Yet, previous interpretations held that the majority of CLIP's ~4.4 million km³ volume had already been emplaced earlier, between 94 and 89 Ma (Snow et al., 2005; Kuroda et al., 2007; Turgeon and Creaser, 2008; Kerr, 2014; Percival et al., 2024).

To evaluate a possible correlation between OAE3 and CLIP volcanism, we first examine the timing of CLIP volcanism. Based on several criteria of reliability and precision, Jiang et al. (2023) critically reevaluated the statistical robustness of all the $^{40}Ar/^{39}Ar$ and U-Pb ages of the CLIP and 17 other Phanerozoic LIPs. Of the initial 65 unfiltered CLIP ages, only 17 filtered ages were considered statistically robust. The filtered ages support the previous view that the CLIP formed over a prolonged period (~30 Ma; e.g., Loewen et al., 2013), consistent with recent geophysical studies suggesting that this extended LIP activity was largely controlled by seafloor spreading (e.g., Ramos et al., 2025). Importantly, both the filtered and unfiltered ages, when plotted in KDE diagrams, reveal a key feature of CLIP volcanism (Fig. 6 and Fig. S3): a peak eruptive phase beginning shortly before 88 Ma. Some filtered KDE curves of LIPs in Fig. 6B are based on fewer than 10 ages, but they closely match the unfiltered curves (all $n > 10$; Fig. S3), indicating that the age peaks are not an artifact of small sample sizes. The age pattern of the CLIP is consistent with the earlier compilation of Loewen et al. (2013), which identified a peak activity between 90 and 85 Ma. This peak is further supported by estimates of global LIP magma flux, with the 90–85 Ma interval (~3 km³/yr) representing the fourth highest of the Cretaceous, following the 125–120 Ma (~12 km³/yr), 100–95 Ma (~4.3 km³/yr), and 135–130 Ma (~4.2 km³/yr) intervals (Coffin et al., 2006). Moreover, the KDE of filtered CLIP ages shows no significant peak in the Cenomanian–Turonian; instead, the peak eruptive phases in the 98–92 Ma interval are observed in the Kerguelen and High Arctic LIPs (Fig. 6B). These filtered ages cast doubt on the view that CLIP volcanism played a significant role in triggering OAE2 (93.9 Ma), suggesting that the bulk of the CLIP may have erupted entirely after the event (Kasbohm et al., 2021). Recent studies have instead identified the Kerguelen and High Arctic LIPs as the primary contributors to OAE2 (e.g., Dummann et al., 2024; Walker-Trivett et al., 2024).

If the CLIP was indeed the primary driver of OAE3, then multiple geochemical and sedimentological proxies–such as shifts in carbon isotope ratios, trace metal enrichments, and black shale deposits–should align temporally within the Coniacian–Santonian interval. Fig. 6 shows a clear temporal correlation among OAE3a, the peak phase of the CLIP, and the deposition of the Loma Chumico black shales, all of which began between 89 and 88 Ma. Moreover, positive shifts in several global carbon isotope curves indicate that the carbon cycle perturbation during the OAE3 subevents was recorded in both marine and continental environments worldwide (Mansour and Wagreich, 2022; Richey et al., 2023). Our new results from Holes 700B and U1513A show that Hg values are consistent across boreholes–i.e., no local faulting (Ciesielski and Kristoffersen, 1988; Huber et al., 2019) could account for the Hg enrichments

(e.g., Zhang et al., 2014)–and that they peaked immediately before (~0.1 Ma) the East Cliff event. This event was followed by the onset of the largest positive carbon isotope excursions in the Coniacian, which include the White Fall and Kingsdown events (Fig. 6; Jarvis et al., 2006), between which we infer that OAE3a took place.

Recently, Grasby et al. (2025) identified OAE3 in organic-rich rocks of the Smoking Hills Fm. in the Western Interior Seaway (Fig. 1A). They attribute the high Hg abundances (up to 370 ppb; Fig. 6B), typically associated with LIP volcanism (Percival et al., 2024), to regional arc volcanism, supported by the presence of arc-derived bentonites. This interpretation is based on the supposedly low magma output and predominantly submarine nature of known LIPs from that period. However, bentonites in the studied section were not analzyed for Hg contents and are not confined to the Hg-enriched intervals–they also appear in the overlying, less Hg-rich Mason Fm. Scaife et al. (2017) observed in other parts of the Western Interior Seaway that bentonite deposits did not affect the Hg levels of adjacent strata. Additionally, filtered ages of the peak CLIP eruption (Fig. 6; Jiang et al., 2023), along with evidence for a subaerial CLIP phase around 88 Ma (Buchs et al., 2018), may offer an alternative explanation for the Hg enrichments reported here and by Grasby et al. (2025). We observe a striking similarity between the Hg curves of Holes 700B/U1513A and that of the Smoking Hills (Fig. 6): all curves peak shortly (~0.5 Ma) before OAE3a, remain relatively high during the event, and decline shortly afterward. This pattern suggests that Hg enrichments in marine sediments began to occur globally between 89 and 88 Ma, shortly preceding the onset of OAE3.

Subaerial and submarine eruptions of the CLIP could have perturbed not only the global Hg cycle (e.g., Percival et al., 2024), as documented in Holes 700B/U1513A and in the Western Interior Seaway, but also enhanced the environmental and climatic changes (e.g., Mather and Schmidt, 2021) reported during OAE3. A significant eruption of the CLIP during the Coniacian–Santonian would be consistent with an estimated 1.5- to 2-fold increase in atmospheric CO_2 concentrations near the Coniacian–Santonian boundary–similar to the rise observed following OAE2 (based on fossil leaves: Barral et al., 2017; and on phytoplankton: Witkowski et al., 2018). Using the offset between global $\delta^{13}C_{org}$ and $\delta^{13}C_{carb}$ curves, Mansour and Wagreich (2022) estimated that atmospheric CO_2 concentrations increased at the onset of OAE3a, possibly as a result of LIP activity.

Indeed, OAE3 had a much more limited environmental impact compared to earlier OAEs. Unlike OAE2, it lacked the multiple LIP eruptions (Fig. 6B) that likely produced rates of magma effusion high enough to trigger a short-lived, major environmental crisis (e.g., Ernst and Youbi, 2017). Instead, the prolonged eruption of the CLIP, which lasted approximately 4 Ma during its main peak, may have been significant enough to sustain the episodic formation of black shales and to cause a mild disturbance to the global carbon cycle, though not severe enough to trigger mass extinctions. Although further research is needed to trace the influence of LIP magmatism during OAE3–such as elemental and isotopic analyses of sedimentary rocks–the regional occurrence of organic-rich sequences overlying and in places interbedded with the peak phase of the CLIP eruption supports a causal relationship. Finally, higher-precision ages of the CLIP are needed to determine whether its peak phase may be subdivided into three pulses that were synchronous with the three subevents of OAE3.

6. Conclusions

The Loma Chumico Fm. reveals that black shales were deposited in the forearc basin of Costa Rica during OAE3a. Radiolarian biostratigraphy and zircon U–Pb geochronology of tuffs and volcaniclastic rocks intercalated with the OAE3a black shales indicate deposition around 88 Ma (middle to late Coniacian). In the early to middle Coniacian interval of ODP Hole 700B and IODP Hole U1513A, the largest Hg enrichments immediately precede the onset of the greatest positive $\delta^{13}C_{carb}$ excursion of the Coniacian, which peaks at the White Fall and Kingsdown events in the English Chalk reference curve (i.e., Jarvis et al., 2006). Although several LIPs were active during OAE3, the CLIP was the only one that peaked during the anoxic event, supporting the interpretation that its subaerial and submarine eruptions could have intensified global carbon- and mercury-cycle perturbations through atmospheric and oceanic dispersal of large volumes of magmatic material and gases. When combined with recently revised $^{40}Ar/^{39}Ar$ ages of the CLIP and new Hg data from Holes 700B and U1513A, the results from the Loma Chumico Fm. suggest that initial peak CLIP magmatism between 89 and 88 Ma likely triggered the environmental disturbances associated with OAE3, including regional marine anoxia and deposition of black shales.

Acknowledgements

We thank Roger Blanco, Maria Marta Chavarria, and Percy Denyer for providing us with the documentation for sample exportation in 2010, 2013, and 2015. We thank Philippe Weber, Maria I. Sandoval, and David Laurent for their help in the field. We thank the International Ocean Discovery Program (IODP) and the Ocean Drilling Program (ODP) for providing the core samples used in this study. We thank Rie Hori for organizing the sampling of cores 1513 at the Kochi Core Center. We thank Emma Duris et Romain Goncerut for their help with mercury and total organic carbon analysis. We thank Benita Putlitz for her help with zircon separation. We thank Jack Gillespie for his help with the polishing of zircon samples. This research was supported by funds of the Swiss National Science Foundation (grants 125130, 143894, and 162670) granted to P.O.B. and the Herbette Foundation at the University of Lausanne.

Supplementary materials

Supplementary material associated with this article can be found in the online version at (link to be provided).

Data availability

The data have been attached as a Supplementary Material.

References

Andjić, G., Baumgartner-Mora, C., Baumgartner, P.O., Petrizzo, M.R., Vennemann, T., Paul, A.N., Lorenzo, V., 2025. Demise of the Barra Honda carbonate shoal (Costa Rica) at the Paleocene-Eocene boundary linked to climate change and forearc tectonics. Geochem. Geophys. Geosyst. 26, e2024GC012080. https://doi.org/10.1029/2024GC012080.

Andjić, G., Baumgartner, P.O., Baumgartner-Mora, C., 2018. Rapid vertical motions and formation of volcanic arc gaps: Plateau collision recorded in the forearc geological evolution (Costa Rica margin). Basin Res. 30 (5), 863–894. https://doi.org/10.1111/bre.12284.

Andjić, G., Baumgartner, P.O., Baumgartner-Mora, C., 2019. Collision of the Caribbean large igneous province with the Americas: Earliest evidence from the Forearc of Costa Rica. Geol. Soc. Am. Bull. 131 (9–10), 1555–1580. https://doi.org/10.1130/B35037.1.

Bandini, A.N., Flores, K., Baumgartner, P.O., Jackett, S.J., and Denyer, P., 2008. Late Cretaceous and Paleogene Radiolaria from the Nicoya Peninsula, Costa Rica: A tectonostratigraphic application. Stratigraphy 5, 3–21.

Barclay, R., McElwain, J., Sageman, B., 2010. Carbon sequestration activated by a volcanic CO2 pulse during Ocean Anoxic Event 2. Nature Geosci. 3, 205–208. https://doi.org/10.1038/ngeo757.

Barral, A., Gomez, B., Fourel, F., Daviero-Gomez, V., Lécuyer, C., 2017. CO2 and temperature decoupling at the million-year scale during the Cretaceous Greenhouse. Sci. Rep. 7, 8310. https://doi.org/10.1038/s41598-017-08234-0.

Baumgartner, P.O., Escuder-Viruete, J., Andjić, G., Baumgartner-Mora, C., 2024. El volcanismo del Plateau Oceánico Caribeño-Colombiano (CLIP) y su impacto paleoambiental durante los eventos OAE3 (Coniaciense-Santoniense): correlación directa mediante biocronología de radiolarios. XI Congreso Geológico de España, 966–969.

Baumgartner, P.O., Flores, K., Bandini, A.N., Girault, F., and Cruz, D., 2008. Upper Triassic to Cretaceous radiolaria from Nicaragua and northern Costa Rica: The Mesquito composite oceanic terrane. Ofioliti, v. 33, p. 1–19. https://doi.org/10.4454/ofioliti.v33i1.356.

Bomou, B., De Kaenel, E., Thibault, N.R., Spangenberg, J.E., Gertsch, B., Frijia, G., Adatte, T., 2025. Palaeoenvironment and palaeclimatic study of the Olazagutia (Spain) and Ten Mile Creek-Arbor Park (USA) sections during the Coniacian–Santonian interval. Geol. Soc. London Spec. Publ. 545, 219–245. https://doi.org/10.1144/SP545-2023-178.

Bragina, L., Bragin, N., Tsiolakis, E., Symeou, V., Papadimitriou, N., Proshina, P., 2021. Late Cretaceous (Coniacian) age of the Perapedhi Formation in the Akamas Peninsula, Cyprus. Cretaceous Res. 127, 104912. https://doi.org/10.1016/j.cretres.2021.104912.

Bragina, L.G., 2025. A New Radiolarian Species Pseudodictyomitra coronata sp. nov. from the Coniacian–Santonian Deposits of the Perapedhi Formation, Cyprus. Paleontol. J. 59, 8–16. https://doi.org/10.1134/S0031030124601452.

Buchs, D.M., Kerr, A.C., Brims, J.C., Zapata-Villada, J.P., Correa-Restrepo, T., Rodríguez, G., 2018. Evidence for subaerial development of the Caribbean oceanic plateau in the Late Cretaceous and palaeo-environmental implications. Earth Planet. Sci. Lett. 499, 62–73. https://doi.org/10.1016/j.epsl.2018.07.020.

Carvajal-Arenas, L.C., Torrado, L., Mann, P., English, J., 2020. Basin modeling of Late Cretaceous/Mio-Pliocene (.) petroleum system of the deep-water eastern Colombian Basin and South Caribbean Deformed Belt. Mar. Pet. Geol. 121. 104511. https://doi.org/10.1016/j.marpetgeo.2020.104511.

Ciesielski, P.F., Kristoffersen, Y., 1988. In: Proceedings of the Ocean Drilling Program, Initial Reports 114. Ocean Drilling Program, College Station, TX, pp. 1–815.

Coffin, M.F., Duncan, R.A., Eldholm, O., Fitton, J.G., Frey, F.A., Larsen, H.C., Mahoney, J.J., Saunders, A.D., Schlich, R., Wallace, P.J., 2006. Large igneous provinces and scientific ocean drilling: status quo and a look ahead. Oceanography 19, 150–160. https://doi.org/10.5670/oceanog.2006.13.

De Romero, L.M., Truskowski, I.M., Bralower, T.J., Bergen, J.A., Odreman, O., Zachos, J.C., Galea-Alvarez, F.A., 2003. An integrated calcareous microfossil biostratigraphic and carbon-isotope stratigraphic framework for the La Luna Formation, western Venezuela. Palaios 18 (4–5), 349–366. https://doi.org/10.1669/0883-1351(2003)018<0349:AICMBA>2.0.CO;2.

Dickinson, W.R., Gehrels, G.E., 2009. Use of U-Pb ages of detrital zircons to infer maximum depositional ages of strata: a test against a Colorado Plateau Mesozoic database. Earth Planet. Sci. Lett. 288, 115e125. https://doi.org/10.1016/j.epsl.2009.09.013.

Dummann, W., Wennrich, V., Schröder-Adams, C.J., Leicher, N., Herrle, J.O., 2024. Ash deposits link Oceanic Anoxic Event 2 to High Arctic volcanism. Geology 52 (12), 927–932. https://doi.org/10.1130/G52368.1.

Dürkefälden, A., Hoernle, K., Hauff, F., Wartho, J.-A., van den Bogaard, P., Werner, R., 2019. Age and geochemistry of the Beata Ridge: primary formation during the main phase (~89 Ma) of the Caribbean Large Igneous Province. Lithos, 328–329, 69–87. https://doi.org/10.1016/j.lithos.2018.12.021.

Edgar, T.N., Saunders, J.B., Donnelly, T.W., Schneidermann, N., Maurrasse, F., Bolli, H.M., Hay, W.W., Riedel, W.R., Premoli Silva, I., Boyce, R.E., Prell, W., 1973. Initial Reports of the Deep-Sea Drilling Project 15. U.S. Government Printing Office. https://doi.org/10.2973/dsdp.proc.15.108.1973.

Erlich, R., Astorga, A., Soler, Z., Patts, M., Palmer, E., 1996. Paleoceanography of organic-rich rocks of the Loma Chumico Formation of Costa Rica, Late Cretaceous, eastern Pacific. Sedimentology 43, 691–718. https://doi.org /10.1111/j.1365-3091.1996.tb02021.x.

Ernst, R.E., Youbi, N., 2017. How large Igneous Provinces affect global climate, sometimes cause mass extinctions, and represent natural markers in the geological record. Palaeogeogr. Palaeoclimatol. Palaeoecol. 478, 30–52. https://doi.org/10.1016/j.palaeo.2017.03.014.

Grasby, S.E., Crowley, J.L., Mohr, M.T., Percival, J.B., Ardakani, O.H., Galloway, J., Bringué, M., Smith, R.I., Yuan, W., 2025. Oceanic anoxic event 3 in Arctic Canada–Arc volcanism and ocean fertilization drove anoxia. Geol. Soc. Am. Bull. 137, 411–426. https://doi.org/10.1130/B37632.1.

Grasby, S.E., Them, T.R., II., Chen, Z., Yin, R., Ardakani, O.H., 2019. Mercury as a proxy for volcanic emissions in the geologic record. Earth Sci. Rev. 196, 102880. https://doi.org/10.1016/j.earscirev.2019.102880.

Hauff, F., Hoernle, K., van den Bogaard, P., Alvarado, G., Garbe-Schönberg, D., 2000. Age and geochemistry of basaltic complexes in western Costa Rica: Contributions to the geotectonic evolution of Central America. Geochem. Geophys. Geosyst. 1 (5). https://doi.org/10.1029/1999GC000020.

Huber, B.T., Hobbs, R.W., Bogus, K.A., Batenburg, S.J., Brumsack, H.-J., do Monte Guerra, R., et al. & the Expedition 369 Scientists, 2019. Site U1513. In: Hobbs, R.W., Huber, B.T. Bogus, K.A. (Eds.), Australia Cretaceous Climate and Tectonics. Proceedings of the International Ocean Discovery Program (Vol. 369). International Ocean Discovery Program. https://doi.org/10.14379/iodp.proc.369.104.2019.

Jarvis, I., Gale, A.S., Jenkyns, H.C., Pearce, M.A., 2006. Secular variation in Late Cretaceous carbon isotopes: a new δ13C carbonate reference curve for the Cenomanian–Campanian (99.6–70.6 Ma). Geol. Mag. 143, 561–608. https://doi.org/10.1017/S0016756806002421.

Jenkyns, H.C., 1980. Cretaceous anoxic events: from continents to oceans. J. Geol. Soc. 137, 171–188. https://doi.org/10.1144/gsjgs.137.2.0171.

Jenkyns, H.C., 2010. Geochemistry of Oceanic Anoxic Events. Geochem. Geophys. Geosyst. 11 (3), Q03004. https://doi.org/10.1029/2009GC002788.

Jiang, Q., Jourdan, F., Olierook, H.K.H., Merle, R.E., 2023. An appraisal of the ages of Phanerozoic large igneous provinces. Earth Sci. Rev. 237, 104314. https://doi.org/10.1016/j.earscirev.2023.104314.

Joo, Y.J., Sageman, B.B., 2014. Cenomanian to Campanian carbon isotope chemostratigraphy from the Western Interior Basin, U.S.A. J. Sed. Res. 84, 529–542. https://doi.org/10.2110/jsr.2014.38.

Kasbohm, J., Schoene, B., Burgess, S., 2021. Radiometric constraints on the timing, tempo, and effects of Large Igneous Province emplacement. In: Ernst, R.E., Dickson, A.J., Bekker, A. (Eds.), Large Igneous Provinces: A Driver of Global Environmental and Biotic Changes. Geophys. Monogr. 255, pp. 27–82. https://doi.org/10.1002/9781119507444.ch2.

Kerr, A.C., 2014. Oceanic plateaus. In: Holland, H., and Turekian, K. (Eds.), Treatise on Geochemistry (2nd edition), The Crust, 4. Amsterdam, The Netherlands, Elsevier, p. 631–667.

Kolarsky, R.A., Mann, P., Monechi, P., Meyerhoff, H.D., and Pessagno, E.A., Jr., 1995, Stratigraphic development of southwestern Panama as determined from integration of marine seismic data and onshore geology. In: Mann, P. (Ed.), Geologic and Tectonic Development of the Caribbean Plate Boundary in Southern Central America. Geol. Soc. Am. Spec. Paper, 295, pp. 159–200, https://doi.org /10.1130 /SPE295-p159.

679 Kuroda, J., Ogawa, N.O., Tanimizu, M., Coffin, M.F., Tokuyama, H., Kitazato, H., Ohkouchi, N., 2007.
680 Contemporaneous massive subaerial volcanism and Late Cretaceous oceanic anoxic event 2. Earth
681 Planet. Sci. Lett. 256, 211–223. https://doi.org/10.1016/j.epsl.2007.01.027.
682
683 Leckie, R.M., Bralower, T. J., Cashman, R., 2002. Oceanic anoxic events and plankton evolution: Biotic
684 response to tectonic forcing during the mid-Cretaceous. Paleoceanography 17 (3).
685 https://doi.org/10.1029/2001PA000623.
686
687 Loewen, M.W., Duncan, R.A., Kent, A.J.R., Krawl, K., 2013. Prolonged plume volcanism in the
688 Caribbean Large Igneous Province: New insights from Curaçao and Haiti. Geochem. Geophys. Geosyst.
689 Geosystems 14, 4241–4259. https://doi.org/10.1002/ggge.20273.
690
691 McArthur, J.M., Howarth, R.J., Shields, G.A., Zhou, Y., 2020. In: Gradstein, F.M., Ogg, J. G., Schmitz,
692 M.D., Ogg, G.M. (Eds.), Sr-Isotope Stratigraphy, Chapter 7, Vol. 1, pp. 211–238. A Geologic Time
693 Scale 2020, Elsevier.
694
695 Mansour, A., Wagreich, M., 2022. Earth system changes during the cooling greenhouse phase of the
696 Late Cretaceous: Coniacian–Santonian OAE3 subevents and fundamental variations in organic carbon
697 deposition: Earth Sci. Rev. 229, 104022. https://doi.org/10.1016/j.earscirev.2022.104022.
698
699 Mather, T.A., Schmidt, A., 2021. Environmental Effects of Volcanic Volatile Fluxes From Subaerial
700 Large Igneous Provinces. In: Ernst, R.E., Dickson, A.J., Bekker, A. (Eds.), Large Igneous Provinces: A
701 Driver of Global Environmental and Biotic Changes. Geophys. Monogr. 255, pp. 103–116.
702 https://doi.org/10.1002/9781119507444.ch4.
703
704 Miniati, F., Jarvis, I., Monkenbusch, J., Erba, E., Ullmann, C.V., Thibault, N., 2025. Upper Cretaceous
705 (upper Turonian–lower Campanian) calcareous nannofossils and carbon isotopes from Seaford Head
706 (southern England): critical appraisal of biozones and correlation to GSSPs. Cretaceous Res.106214.
707 https://doi.org/10.1016/j.cretres.2025.106214.
708
709 Noroña Muñoz, E., Ulianov, A., Spikings, R. Gerdes, A., Berger, A., Abrecht, J., Wiederkehr, M.,
710 Schaltegger, U., 2025. An Ordovician magmatic and metamorphic event in the pre-Mesozoic basement
711 of the Central Alps (Aar Massif and Gotthard Nappe). Swiss J. Geosci. 118, 19 (2025).
712 https://doi.org/10.1186/s00015-025-00492-9
713
714 O'Dogherty, L., Carter, E.S., Dumitrica, P., Goričan, Š., De Wever, P., Bandini, A.N., Baumgartner,
715 P.O., Matsuoka, A., 2009. Catalogue of Mesozoic radiolarian genera. Part 2: Jurassic-Cretaceous.
716 Geodiversitas 31, 271–356. https://doi.org/10.5252/g2009n2a4.
717
718 Ogg, J.G., Ogg, G.M., Gradstein, F.M., 2016. 13 – Cretaceous. In: James G. Ogg, Gabi M. Ogg, Felix
719 M. Gradstein (Eds.), A Concise Geologic Time Scale, 2016. Amsterdam, The Netherlands, Elsevier,
720 pp. 167–186. https://doi.org/10.1016/B978-0-444-59467-9.00013-3.
721
722 Percival, L.M.E., Matsumoto, H., Callegaro, S., Erba, E., Kerr, A.C., Mutterlose, J., Suzuki, K., 2024.
723 Cretaceous large igneous provinces: From volcanic formation to environmental catastrophes and

724 biological crises. Geol. Soc. London Spec. Publ. 544, 299–342. https://doi.org/10.1144 /SP544-2023-
725 88.
726
727 Petrizzo, M.R., Huber, B.T., Falzoni, F., MacLeod, K.G., 2020. Changes in biogeographic distribution
728 patterns of southern mid-to high latitude planktonic foraminifera during the Late Cretaceous hot to cool
729 greenhouse climate transition. Cretaceous Res. 115, 104547.
730 https://doi.org/10.1016/j.cretres.2020.104547.
731
732 Petrizzo, M.R., MacLeod, K.G., Watkins, D.K., Wolfgring, E., Huber, B.T., 2022. Late Cretaceous
733 paleoceanographic evolution and the onset of cooling in the Santonian at southern high latitudes (IODP
734 Site U1513, SE Indian Ocean). Paleoceanogr. Paleoclimatol 37, e2021PA004353.
735 https://doi.org/10.1029/2021PA004353.
736
737 Prauss, M.L., 2015. Marine palynology of the Oceanic Anoxic Event 3 (OAE3, Coniacian-Santonian)
738 at Tarfaya, Morocco, NW Africa - transition from preservation to production controlled accumulation
739 of marine organic carbon. Cretac. Res. 53, 19–37. https://doi.org/10.1016/j.cretres.2014.10.005.
740
741 Ramos, J.P., Mann, P., Carvajal-Arenas, L.C., 2025. Crustal structure and tectonic origin of Late
742 Cretaceous oceanic crust and adjacent Caribbean Large Igneous Province in the Colombian Basin.
743 Geochem. Geophys. Geosyst. 26, e2024GC011602. https://doi.org/10.1029/2024GC011602.
744
745 Richey, J.D., Nordt, L., White, J.D. and Breecker, D.O., 2023. ISOORG23: an updated compilation of
746 stable carbon isotope data of terrestrial organic materials for the Cenozoic and Mesozoic. Earth Sci.
747 Rev. 241, 104439. https://doi.org/10.1016/j.earscirev.2023.104439.
748
749 Scaife, J.D., Ruhl, M., Dickson, A.J., Mather, T.A., Jenkyns, H.C., Percival, L.M.E., Hesselbo, S.P.,
750 Cartwright, J., Eldrett, J.S., Bergman, S.C., Minisini, D., 2017. Sedimentary mercury enrichments as a
751 marker for submarine large igneous province volcanism? Evidence from the Mid-Cenomanian event
752 and Oceanic Anoxic Event 2 (Late Cretaceous). Geochem. Geophys. Geosyst. 18, 4253–4275.
753 https://doi.org/10.1002/2017GC007153.
754
755 Boekhout, F., Spikings, R., Sempere, T., Chiaradia, M., Ulianov, A., Schaltegger, U., 2012. Mesozoic
756 arc magmatism along the southern Peruvian margin during Gondwana breakup and dispersal. Lithos
757 146, 48–64. https://doi.org/10.1016/j.lithos.2012.04.015.
758
759 Scotese, C.R., Vérard, C., Burgener, L., Elling, R.P., Kocsis, A.T., 2025. The Cretaceous world: plate
760 tectonics, paleogeography, and paleoclimate. Geol. Soc. London Spec. Publ. 544, 31–202.
761 https://doi.org/10.1144/SP544-2024-28.
762
763 Singer, B.S., Jicha, B.R., Sawyer, D.A., Walaszczyk, I., Landman, N., Sageman, B.B., McKinney, K.C.,
764 2025. A 40Ar/39Ar and U–Pb Timescale for the Cretaceous Western Interior Basin, North America.
765 Geol. Soc. London Spec. Publ. 544, 367–391. https://doi.org/10.1144/SP544-2023-76.
766
767 Sláma, J., Košler, J., Condon, D.J., Crowley, J.L., Gerdes, A., Hanchar, J.M., Horstwood, M.S., Morris,
768 G.A., Nasdala, L., Norberg, N., 2008. Plešovice zircon–A new natural reference material for U–Pb and

769 Hf isotopic microanalysis. Chem. Geol. 249 (1–2), 1–35.
770 https://doi.org/10.1016/j.chemgeo.2007.11.005.
771
772 Snow, L.J., Duncan, R.A., Bralower, T.J., 2005. Trace element abundances in the Rock Canyon
773 Anticline, Pueblo, Colorado, marine sedimentary section and their relationship to Caribbean plateau
774 construction and oxygen anoxic event 2. Paleoceanogr. Paleoclimatol. 20 (3), PA3005.
775 https://doi.org/10.1029/2004PA001093.
776
777 Spötl, C., Vennemann, T.W., 2003. Continuous-flow IRMS analysis of carbonate minerals. Rapid
778 Commun. Mass Spectrom. 17(9), 1004–1006. https://doi.org/10.1002/rcm.1010.
779
780 Tessin, A., Sheldon, N.D., Hendy, I., Chappaz, A., 2016. Iron limitation in the Western Interior Seaway
781 during the Late Cretaceous OAE 3 and its role in phosphorus cycling and enhanced organic matter
782 preservation. Earth Planet. Sci. Lett. 449, 135–144. https://doi.org/10.1016/j.epsl.2016.05.043.
783
784 Thibault, N., Jarvis, I., Voigt, S., Gale, A.S., Attree, K., Jenkyns, H.C., 2016. Astronomical calibration
785 and global correlation of the Santonian (Cretaceous) based on the marine carbon isotope record.
786 Paleoceanography 31, 847–865. https://doi.org/10.1002/2016PA002941.
787
788 Turgeon, S.C., Creaser, R.A., 2008. Cretaceous oceanic anoxic event 2 triggered by a massive magmatic
789 episode. Nature 454, 323–326. https://doi.org/10.1038/nature07076.
790
791 Ulianov, A., Müntener, O., Schaltegger, U., Bussy, F., 2012. The data treatment dependent variability
792 of U–Pb zircon ages obtained using mono-collector, sector field, laser ablation ICPMS. J. Anal. At.
793 Spectrom. 27 (4), 663–676. https://doi.org/10.1039/C2JA10358C.
794
795 Vermeesch, P., 2018. IsoplotR: A free and open toolbox for geochronology. Geosci. Front. 9 (5), 1479–
796 1493. https://doi.org/10.1016/j.gsf.2018.04.001.
797
798 Wagreich, M., 2009. Coniacian-Santonian oceanic red beds and their link to Oceanic Anoxic Event 3.
799 In: Hu, X., Wang, C., Scott, R.W., Wagreich, M., Jansa, L. (Eds.), Cretaceous Oceanic Red Beds:
800 Stratigraphy, Composition, Origins, and Paleoceanographic and Paleoclimatic Significance, 91. SEPM
801 Spec. Pub., pp. 235–242. https://doi.org/10.2110/sepmsp.091.235.
802
803 Wagreich, M., 2012. "OAE 3"- regional Atlantic organic carbon burial during the Coniacian-Santonian.
804 Clim. Past 8, 1447–1455. https://doi.org/10.5194/cp-8-1447-2012.
805
806 Walker-Trivett, C.A., Kender, S., Bogus, K.A., Littler, K., Edvardsen, T., Leng, M.J., Lacey, J., Riding,
807 J.B., Millar, I.L., Wagner, D., 2024. Oceanic Anoxic Event 2 triggered by Kerguelen volcanism. Nat.
808 Commun. 15, 5124. https://doi.org/10.1038/s41467-024-49032-3.
809
810 Weber, P., 2013. Assessing sedimentary evolution by means of Sr-isotope ratios: 3 case studies on the
811 Caribbean Plate (Cretaceous: Nicoya Peninsula, Costa Rica, Tertiary: Hess Rise, and La Désirade,
812 Guadeloupe, France). Ph.D. thesis, University of Lausanne, Lausanne, Switzerland, 176 p.
813

Witkowski, C.R., Weijers, J.W.H., Blais, B., Schouten, S., Sinninghe Damsté, J.S., 2018. Molecular fossils from phytoplankton reveal secular pCO2 trend over the Phanerozoic. Sci. Adv. 4 (11), eaat4556. https://doi.org/10.1126/sciadv.aat4556.

Wright, J.E., Wyld, S.J., 2011. Late Cretaceous subduction initiation on the eastern margin of the Caribbean–Colombian Oceanic Plateau: one Great Arc of the Caribbean (?). Geosphere 7, 468–493. https://doi.org/10.1130/GES00577.1.

Zapata-Villada, J.P., Restrepo, J.J., Cardona-Molina, A., Martens, U., 2017. Geoquímica y geocronología de las rocas volcánicas básicas y el Gabro de Altamira, Cordillera Occidental (Colombia): Registro de ambientes de plateau y arco oceánico superpuestos durante el cretácico. Bol. Cienc. Tierra 39, 13–30. http://dx.doi.org/10.18273/revbol.v39n2-2017001.

Zhang, L., Liu, Y., Guo, L., Yang, D., Fang, Z., Chen, T., Ren, H., Yu, B., 2014. Isotope geochemistry of mercury and its relation to earthquake in the Wenchuan Earthquake Fault Scientific Drilling Project Hole-1 (WFSD-1). Tectonophysics 619–620, 79–85. https://doi.org/10.1016/j.tecto.2013.08.025.

Captions

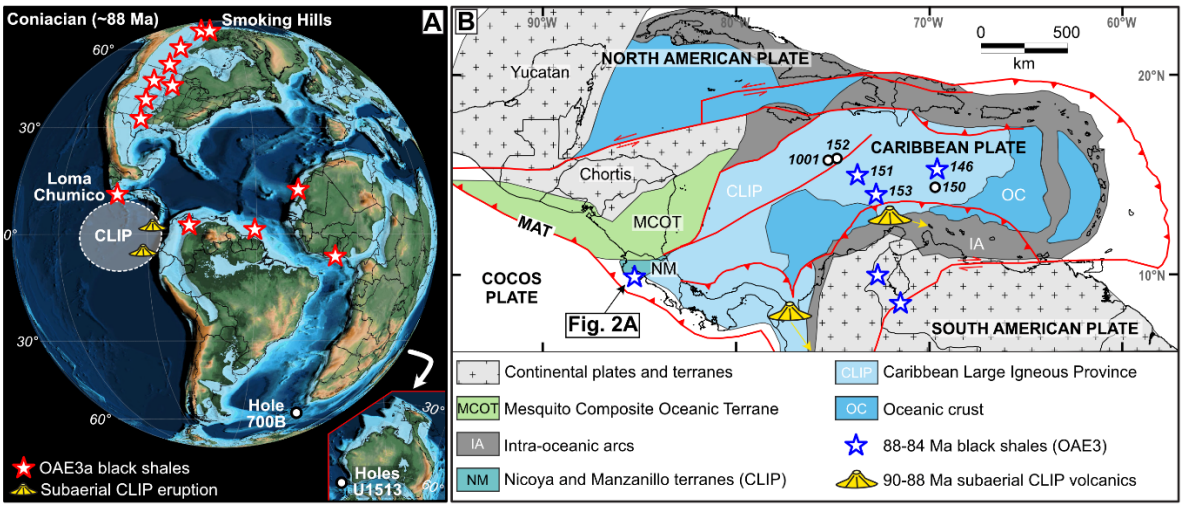

Fig. 1. (A) Coniacian paleogeography (modified after Scotese et al., 2025) showing the location of OAE3a black shales (after Mansour and Wagreich, 2022), including the Loma Chumico Formation (this study), ODP/IODP sites (Ciesielski and Kristoffersen, 1988; Huber et al., 2019), and the Caribbean Large Igneous Province (CLIP). (B) Plate tectonic map illustrating the main units of the Caribbean Plate (modified after Andjić et al., 2025). The location of the Coniacian–Santonian organic-rich rocks is after Carvajal-Arenas et al. (2020) and Mansour and Wagreich (2022). The location of the subaerial CLIP volcanics is after Wright and Wyld (2011) and Buchs et al. (2018). The location of DSDP/ODP sites is after Carvajal-Arenas et al. (2020). MAT = Middle America Trench.

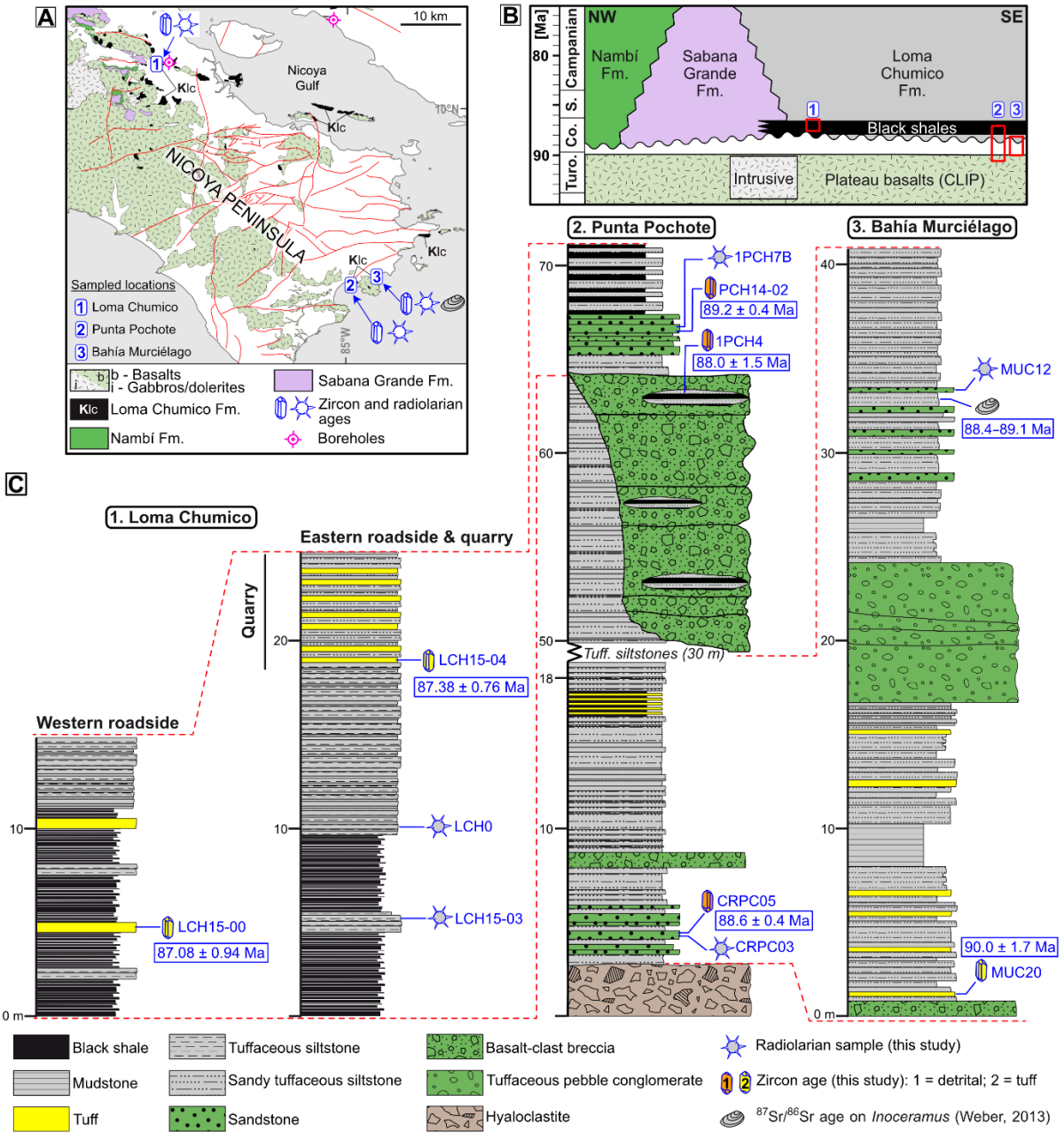

Fig. 2. (A) Geological map of the southern Nicoya Peninsula, Costa Rica (modified after Andjić et al., 2018). The three sampled locations (labelled 1, 2, 3) are those depicted in Fig. 2B and 2C. The Morote-1 borehole is located near our location 1, while the Manzanillo-1 borehole is located on the eastern side of the Nicoya Gulf. (B) Chronostratigraphic chart of the southern Nicoya Peninsula (modified after Andjić et al., 2019). (C) Stratigraphic logs of the lower Loma Chumico Fm. in the Loma Chumico, Punta Pochote, and Bahia Murciélago sections (modified after Andjić et al., 2019). The dashed lines indicate intraformational correlation. The zircon ages are those presented in Fig. 3. GPS coordinates of the sections: (1) Loma Chumico = N 10°03'44.5''/W 85°15'52.4'' (quarry = N 10°03'47.6''/W 85°15'48.5''); (2) Punta Pochote = N 09°44'44.9''/W 84°59'30.6''; (3) Bahia Murciélago = N 09°44'46.9''/W 84°57'19.3''.

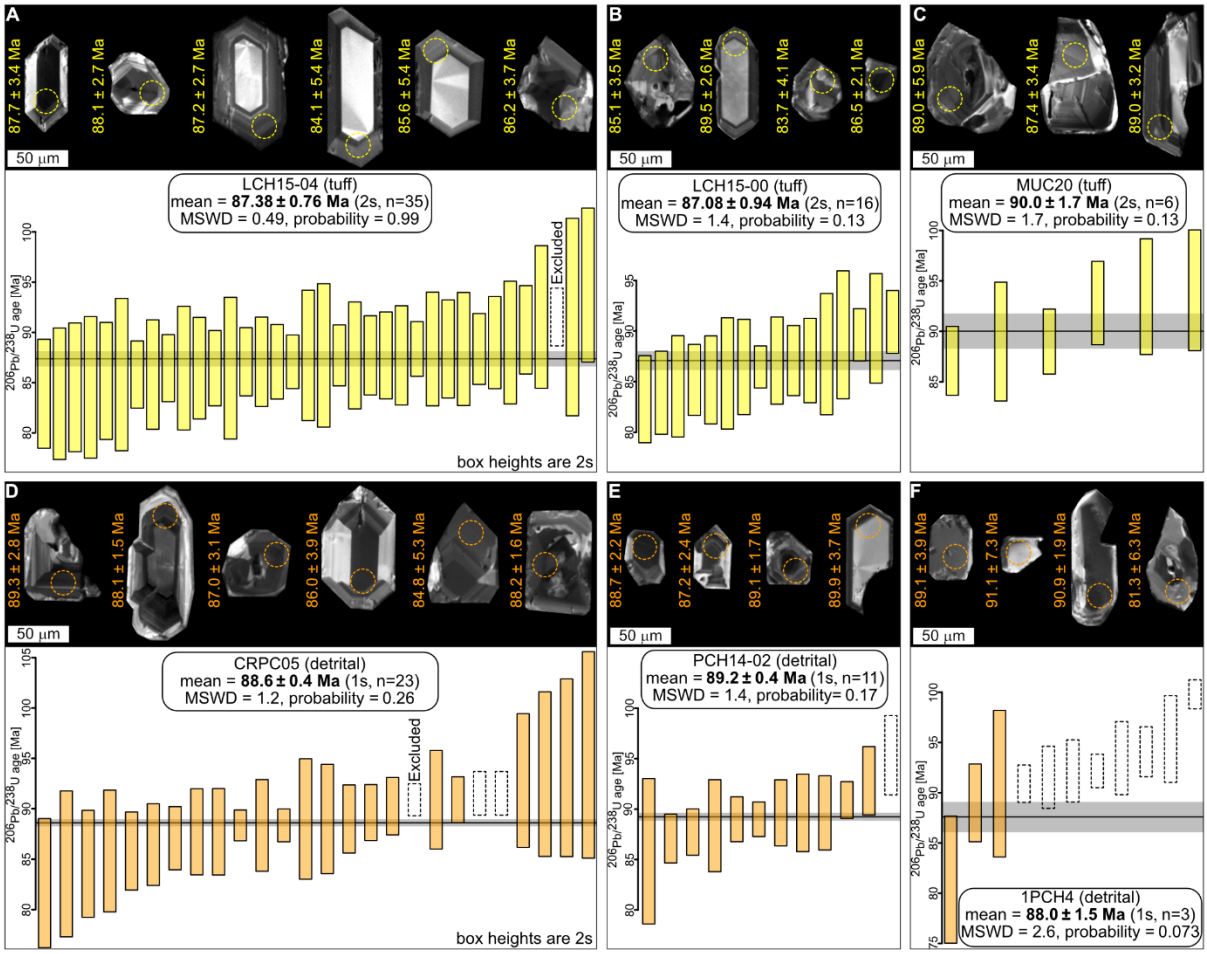

Fig. 3. Plots of ranked $^{206}Pb/^{238}U$ dates from tuff and detrital zircon samples collected in the lower Loma Chumico Fm. Each plot is accompanied by cathodoluminescence images of representative zircons taken with a scanning electron microscope. (A)–(C) Tuff samples. (D)–(F) Detrital samples. The weighted mean $^{206}Pb/^{238}U$ dates of each sample is given with its analytical uncertainty (1s for detrital samples and 2s for tuff samples). Zircon dates excluded from weighted mean calculation are indicated as dashed boxes.

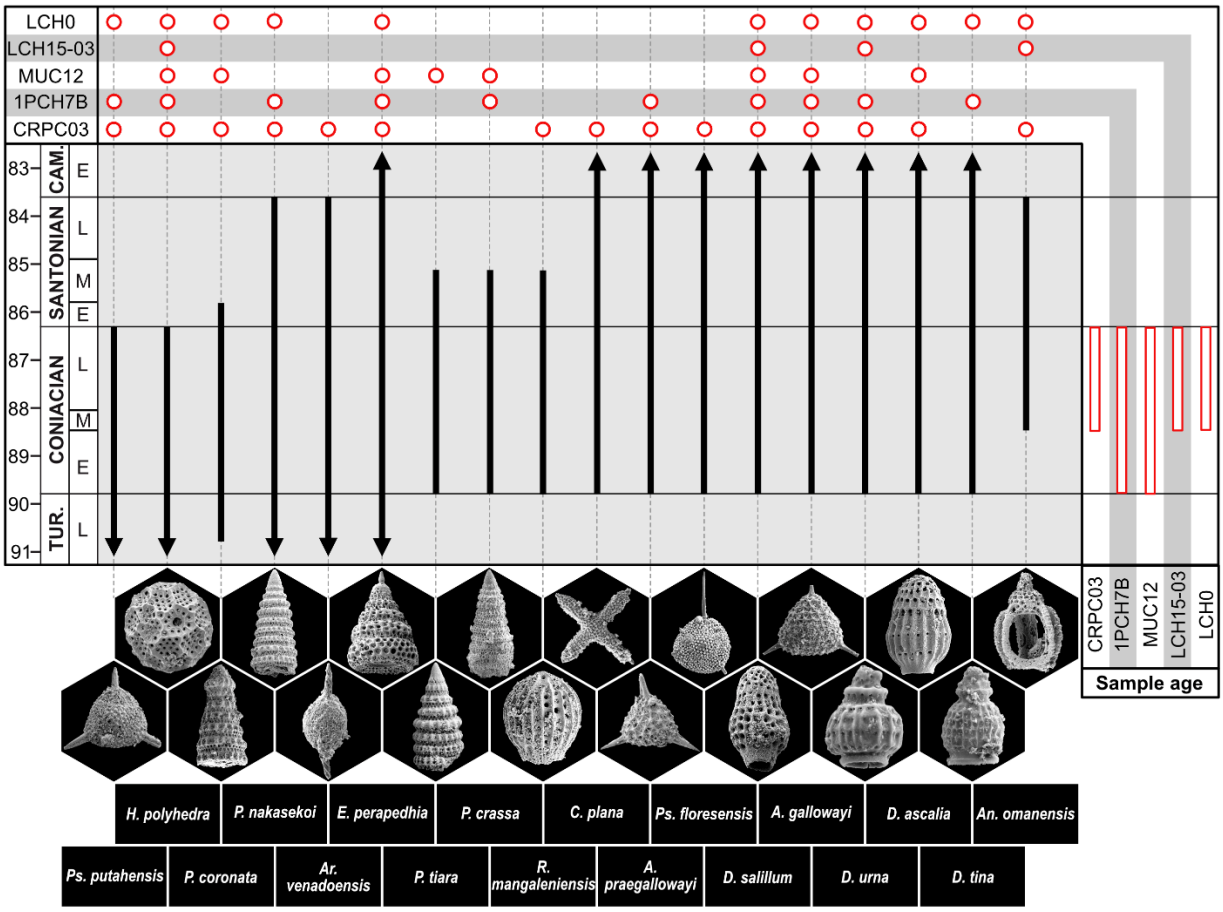

Fig. 4. Age-diagnostic radiolarian species of the lower Loma Chumico Fm. The timescale is after Ogg et al. (2016) and Thibault et al. (2016). Radiolarian age ranges are from O'Dogherty et al. (2009), Andjić et al. (2018, 2019), Bragina et al. (2021), Baumgartner et al. (2024), and Bragina (2025). Genus abbreviations: *A. = Alievium; An. = Annikaella; Ar. = Archaeospongoprunum; C. = Crucella; D. = Dictyoprora; E. = Eostichomitra; H. = Hemicryptocapsa; P. = Pseudodictyomitra; Ps. = Pseudoaulophacus; R. = Rhopalosyringium*. The scale of the radiolarians is indicated below relative to the length of hexagon sides. Side length of hexagons in the upper row, from left to right: (1) 112 µm, (2) 231 µm, (3) 157 µm, (4) 298 µm, (5) 230 µm, (6) 225 µm, (7) 176 µm, (8) 55 µm, (9) 96 µm. Side length of hexagons in the lower row, from left to right: (1) 191 µm, (2) 150 µm, (3) 163 µm, (4) 176 µm, (5) 119 µm, (6) 170 µm, (7) 76 µm, (8) 68 µm, (9) 68 µm. Other abbreviations: Cam. = Campanian; Tur. = Turonian.

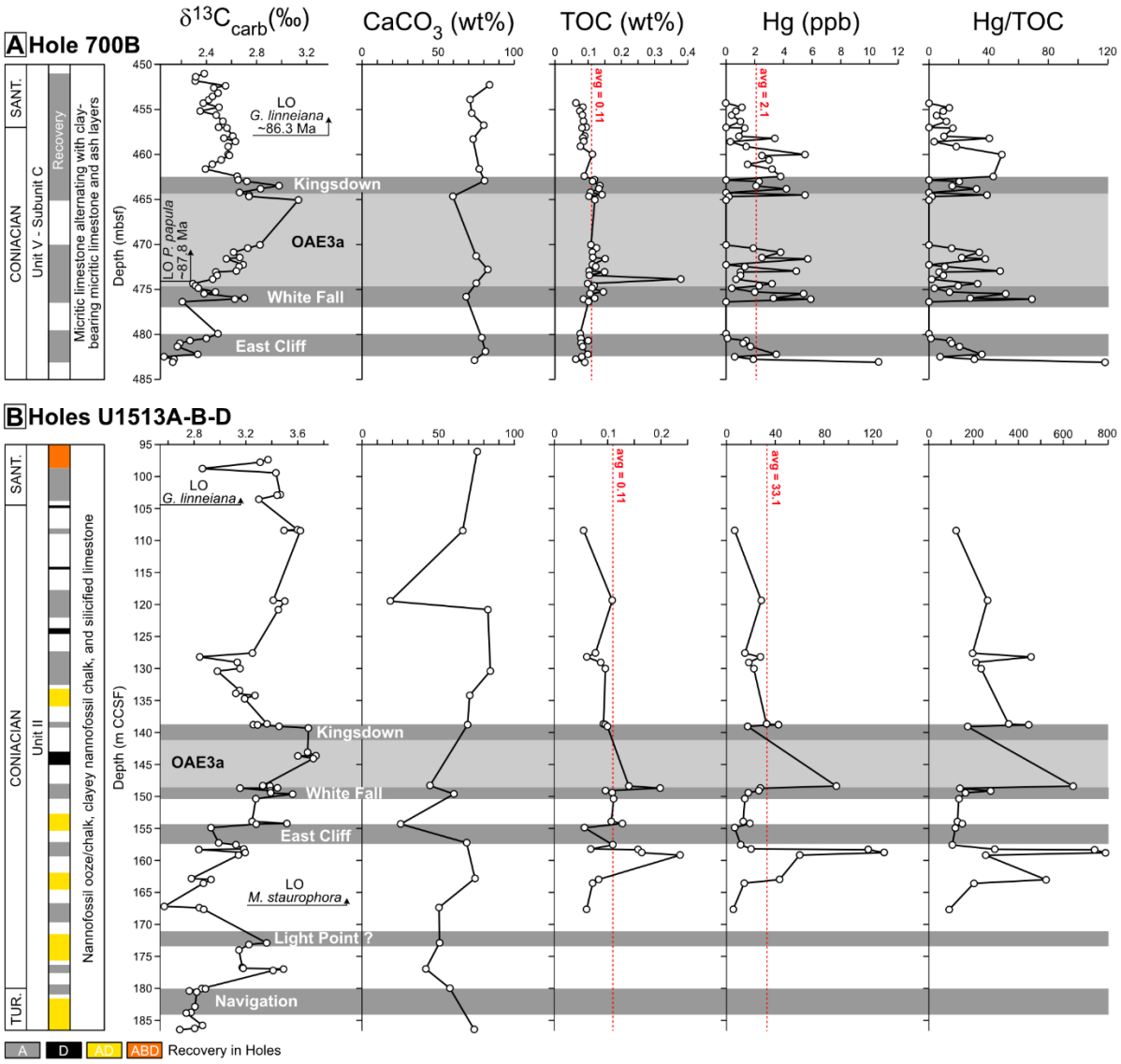

Fig. 5. Data from the Northeast Georgia Rise (Hole 700B) and the Naturaliste Plateau (Holes U1513A, U1513B, U1513D). (A) $\delta^{13}C_{carb}$, TOC, and Hg from this study. $CaCO_3$ from Ciesielski and Kristoffersen (1988). Planktonic foraminifera datums from Petrizzo et al. (2020); the height of the arrows represents the core interval in which the taxa first appear. (B) $\delta^{13}C_{carb}$ from this study and Petrizzo et al. (2022). TOC and Hg from this study (Hole U1513A). $CaCO_3$ from Huber et al. (2019). Planktonic foraminifera datum from Petrizzo et al. (2022). Nannofossil datum from Huber et al. (2019). Carbon isotope events are named after Jarvis et al. (2006). Abbreviations: avg = average; LO = lowest occurrence; Sant. = Santonian; Tur. = Turonian.

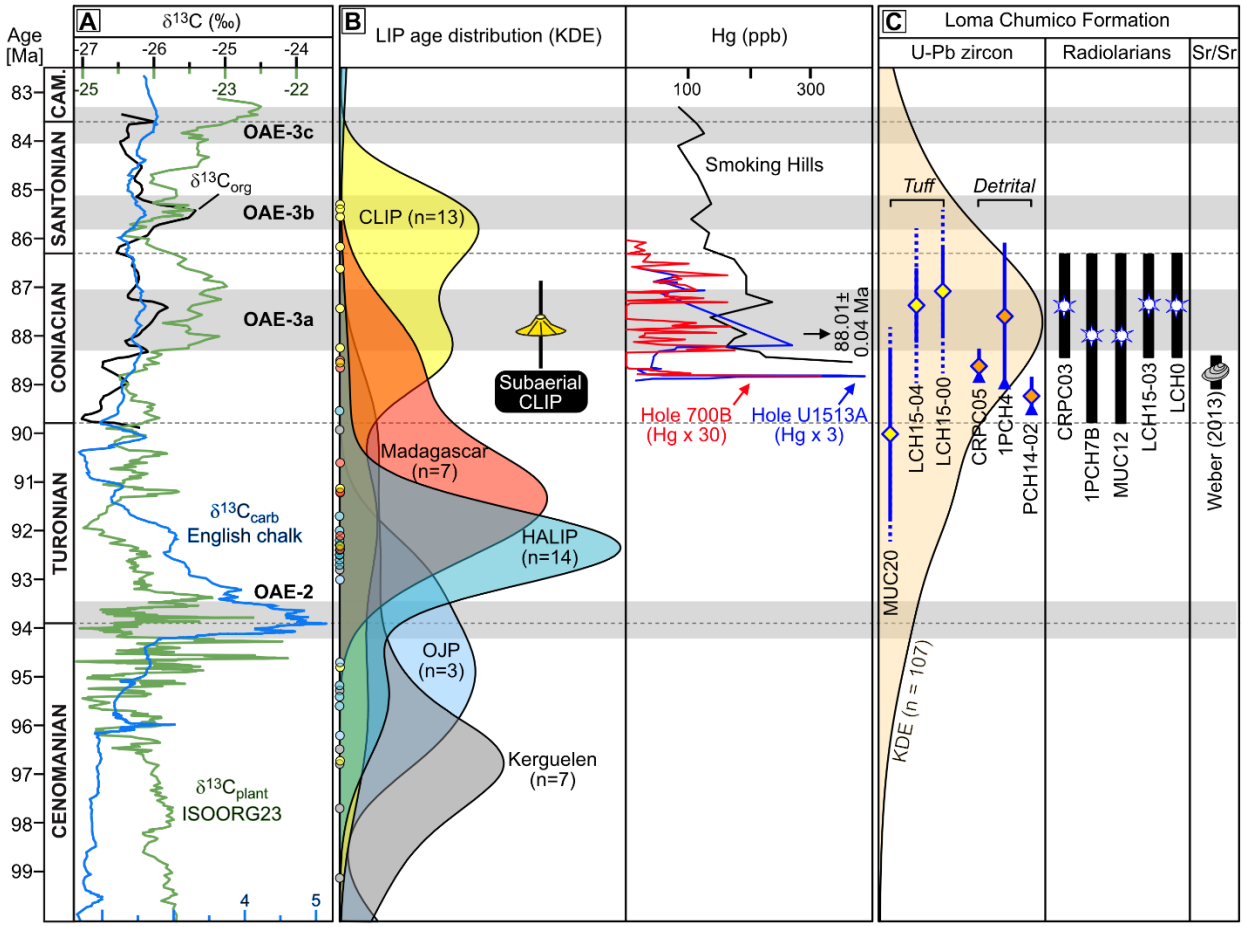

Fig. 6. Temporal correlation among (A) global carbon isotope curves (English Chalk $\delta^{13}C_{carb}$ from Jarvis et al., 2006; $\delta^{13}C_{org}$ after Mansour and Wagreich, 2022; OAE3a-b-c after Mansour and Wagreich, 2022, Joo and Sageman, 2014, and Grasby et al., 2025; 5-point moving average of ISOORG23 $\delta^{13}C_{plant}$ from Richey et al., 2023), (B) Large Igneous Province (LIP) $^{40}Ar/^{39}Ar$ and U-Pb ages (filtered ages from Jiang et al., 2023) combined with Hg data, and (C) biostratigraphic and geochronologic ages of the organic-rich lower Loma Chumico Fm. In (B) and (C), Kernel Density Estimations (KDEs) were computed using IsoplotR (Vermeesch, 2018) and applying a Kernel bandwidth of 1. In (B), some KDE curves of LIPs are based on n < 10 because of dataset filtering; however, they closely resemble the corresponding curves from the unfiltered dataset of Jiang et al. (2023; Fig. S3), in which all sample sizes are n > 10. This similarity indicates that the main features of the age distributions are not artifacts of small sample sizes. The dots on the left side of the KDE curves show the mean ages (without uncertainties) used to compute the curves. In (B), U-Pb ages are only present in the Madagascar (n=3 out of 7) and High Arctic (n=13 out of 14) datasets. In (B), the age of subaerial CLIP eruption is based on the zircon U-Pb age (sample JPA-29) reported in Zapata-Villada et al. (2017) and Buchs et al. (2018): 87.7 ± 0.9 Ma. In (B), new mercury (Hg) data from Holes 700B and U1513A are shown with red and blue curves, respectively. The black Hg curve and ID-TIMS age (88.01 ± 0.04 Ma) are from Grasby et al. (2025; Smoking Hills). In (C), zircon mean ages from tuffs include the systematic uncertainty (dashed lines). Other abbreviations: Cam. = Campanian; HALIP = High Arctic LIP; OAE = Oceanic Anoxic Event; OJP = Ontong Java Plateau.